A molecular switch controls the impact of cholesterol on a Kir channel

Valentina Corradi[a,b] , Anna N. Bukiya[c], Williams E. Miranda[a,b], Meng Cui[d] , Leigh D. Plant[d] , Diomedes E. Logothetis[d,e] , D. Peter Tieleman[a,b,1] , Sergei Y. Noskov[a,b,2] , and Avia Rosenhouse-Dantsker[f,1]

Cholesterol decreases the activity of the majority of ion channels while increasing the activity of only a few, yet it remains unclear how. Here, we used the inwardly rectifying potassium channel Kir3.4, which is up-regulated by cholesterol, as a tool to address this question. Employing mutagenesis and electrophysiology, we discovered a molecular switch that controls the impact of cholesterol on the channel. Through a single point mutation at position 182 in the transmembrane domain of Kir3.4, we converted the cholesterol-driven up-regulation of the channel into down-regulation. Microseconds-long coarse-grained and atomistic molecular dynamics simulations revealed that the effect of the point mutation propagated toward the selectivity filter of the channel whose conformation controls the conductance of the channel. Planar lipid bilayer experiments validated these results, showing that although cholesterol up-regulated Kir3.4 by increasing its open probability, cholesterol down-regulated the mutant by decreasing its conductance. Further studies underscored the role of mutation-specific alterations of cholesterol distribution in proximity to the channel in cholesterol's impact on channel activity, highlighting the role of subtle molecular differences in determining how cholesterol distributes around proteins and affects their function.

G-protein gated inwardly rectifying potassium channels | cholesterol | protein–lipid interactions | ion channel modulation | membrane protein

Cholesterol is a major component of the plasma membrane that plays a key role in a variety of cellular processes (1–3). In particular, alterations in cholesterol levels have been shown to impact the function of an ever-growing number of ion channels (4). However, while the majority of ion channels are down-regulated by cholesterol, only several ion channels are up-regulated by this lipid. Notably, inwardly rectifying potassium (Kir) channels are included in both groups (5–8), providing a unique tool to investigate what determines whether cholesterol will up-regulate or down-regulate the activity of an ion channel.

The observation that the impact of cholesterol varies among different members of the Kir family is puzzling. First, all Kir channels share the same structural features (9–14). Second, sequence identity among Kir channels is relatively high, ranging from 28 to 71%. In particular, the identity between Kir3.1 and Kir3.4 is 50% and the identity between Kir2.1 and Kir3.4 is 48%. Yet, whereas Kir2.1 and Kir3.1* (the homomerically active Kir3.1_F137S pore mutant) (15) are down-regulated by cholesterol (5, 6, 8), Kir3.4* (the Kir3.4_S143T pore mutant that enhances the activity of Kir3.4) (16) is up-regulated (5, 6). Notably, the effect of cholesterol on Kir3.4 dominates the impact of this lipid on the Kir3.1/Kir3.4 channel that underlies atrial K_{ACh} currents; this heterotetrameric channel is also up-regulated by cholesterol (6). Thus, in the present manuscript, we combined experimental and computational approaches to address this intriguing observation and reveal the basis for the up-regulation of this ion channel by cholesterol.

Results

To uncover why the effect of cholesterol on Kir3.4* function is opposite to its effect on Kir2.1 and Kir3.1*, we focused on the sequence differences between these channels to identify regions in Kir3.4* that could potentially affect the impact (up-regulation versus down-regulation) of cholesterol on its function (*SI Appendix,* Fig. S1). The most pronounced difference between Kir3.1* and Kir3.4* is the extended C terminus of Kir3.1*, which is 88 residues longer than the C terminus of Kir3.4*. As we had previously demonstrated that mutations of cytosolic residues of Kir3.4* could abrogate the sensitivity of the channel to cholesterol (5, 6), we tested the effect of replacing the end of the C terminus of Kir3.4*, residues 365 to 419, with the equivalent residues in

Significance

Cholesterol is one of the main components found in plasma membranes and is involved in lipid-dependent signaling enabled by integral membrane proteins such as inwardly rectifying potassium (Kir) channels. Similar to other ion channels, most of the Kir channels are down-regulated by cholesterol. One of the very few notable exceptions is Kir3.4, which is up-regulated by this important lipid. Here, we discovered and characterized a molecular switch that controls the impact (up-regulation vs. down-regulation) of cholesterol on Kir3.4. Our results provide a detailed molecular mechanism of tunable cholesterol regulation of a potassium channel.
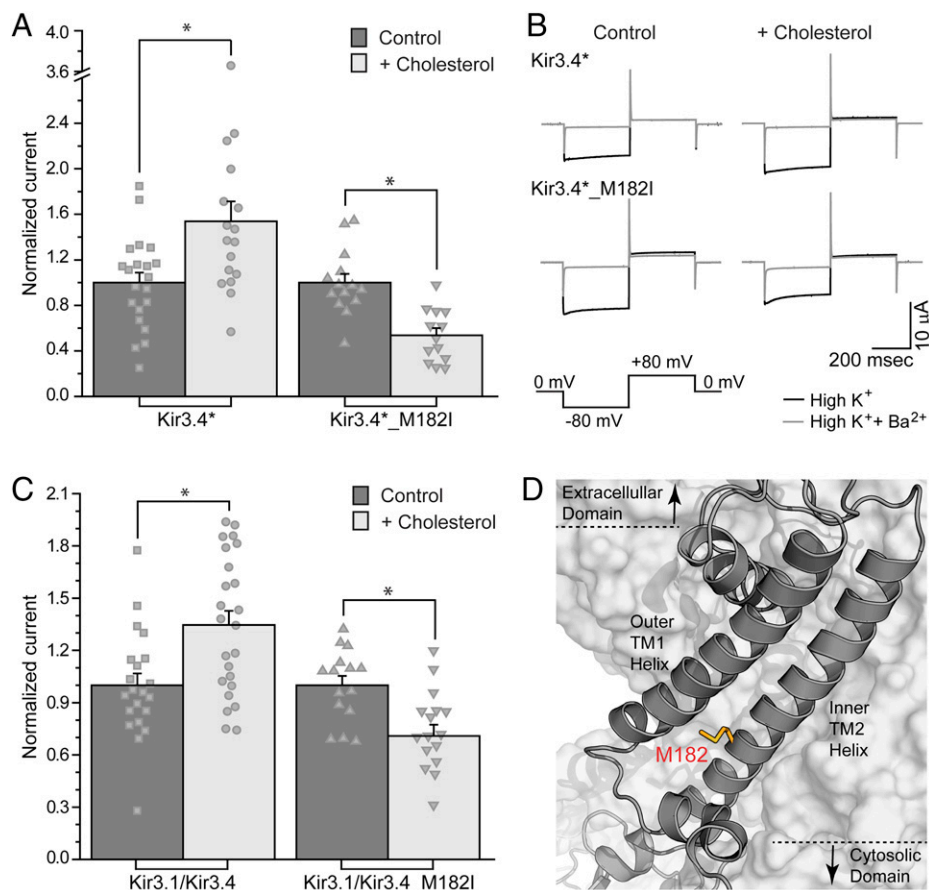
Fig. 1. The M182I mutation switches the cholesterol-driven up-regulation of Kir3.4* into down-regulation. (*A*) Whole-cell basal currents recorded in *Xenopus* oocytes at −80 mV showing the effect of cholesterol enrichment on Kir3.4* and the M182I mutant. The currents were normalized relative to untreated oocytes expressing the same channel (n = 13 to 21). Significant difference is indicated by an asterisk (*$P \leq 0.05$). Error bars, SEM. (*B*) Representative traces of the whole-cell basal currents shown in *A* recorded at −80 mV/+80 mV. The waveform is shown at *Bottom*. (*C*) Whole-cell basal currents recorded in *Xenopus* oocytes at −80 mV showing the effect of cholesterol enrichment on Kir3.1/Kir3.4 and the Kir3.1/Kir3.4_M182I mutant. The currents were normalized relative to untreated oocytes expressing the same channel (n = 15 to 24). Significant difference is indicated by an asterisk (*$P \leq 0.05$). Error bars, SEM. (*D*) Model of the transmembrane domain of subunit D of the last structure in the molecular dynamics simulation of Kir3.4 showing the location of the M182 residue in proximity to the cytosolic domain of the channel. For clarity, the backbones of the four subunits of the tetrameric channel are shown as a gray surface.

Kir3.1*, 359 to 413, and extending it to include the end of the C terminus of Kir3.1*, residues 414 to 501 (*SI Appendix*, Fig. S1, blue-colored residues). As evident in *SI Appendix*, Fig. S2*A*, similarly to Kir3.4*, the resultant chimera was up-regulated by cholesterol, indicating that the extended C terminus of Kir3.1* did not determine the impact of cholesterol on the channel.

Next, we focused on the transmembrane (TM) domain of Kir3.4* as our recent studies have indicated that cholesterol may bind to the TM domain in both Kir2.1 and Kir3.4* (17, 18). Notably, the latter study (18) included mutations of TM residues in Kir3.4* to the corresponding residues in Kir2.1 and/or Kir3.1* (M95L, V96T_T100A, F104M_G105A, L110V, L168F, I190M, L169V, V170F, and V178I, highlighted in *SI Appendix*, Fig. S1). These mutations, however, did not switch the cholesterol-driven up-regulation of Kir3.4* into down-regulation. They either had no effect on the sensitivity of Kir3.4* to cholesterol or abrogated the channel's sensitivity to cholesterol. We thus extended the search to TM residues in Kir3.4* that have not been tested previously and mutated this group of residues that differed from residues located at equivalent positions in Kir2.1 and Kir3.1* to the corresponding residue in Kir2.1 and/or Kir3.1* (T94I, F106S_I107M, M182I, V188I, and I190M) (*SI Appendix*, Figs. S1 and S2*B*). This led to the key discovery of a specific point mutation, M182I, that switched the cholesterol-driven up-regulation of Kir3.4* into

down-regulation (Fig. 1 *A* and *B* and *SI Appendix*, Fig. S2*B*). Notably, the M182I mutation in Kir3.4 also switched the cholesterol-driven up-regulation of the Kir3.1/Kir3.4 heterotetrameric channel into down-regulation (Fig. 1*C*). This residue is located in the inner transmembrane helix of Kir3.4 close to the interface with the cytosolic domain (Fig. 1*D*), and its side chain is facing the space between the inner and outer helices.

To investigate the structural basis for the differential effect of cholesterol on Kir3.4 and its M182I mutant, we simulated the two constructs embedded in a 1-palmitoyl-2-oleoyl-*sn*-glycero-3-phosphoethanolamine (POPE), 1-palmitoyl-2-oleoyl-*sn*-glycero-3-phospho-L-serine (POPS), and cholesterol mixture. As a control, we simulated the constructs in a POPE and POPS binary mixture lacking cholesterol (*Materials and Methods*). For both membranes, with and without cholesterol, 40 μs-long coarse-grained (CG) simulations showed an overall similar lipid composition in proximity to the channel, with no significant differences between the Kir3.4 and Kir3.4_M182I systems (*SI Appendix*, Fig. S3). In particular, in the presence of cholesterol, within the first lipid shell approximated to a 0.7-nm cutoff from the protein, POPS and cholesterol equilibrated to a 1:1 ratio, each representing ∼37% of the total lipid count, while zwitterionic POPE lipids were present at a significantly lower concentration. Occupancy maps calculated as an average over the four subunits for each construct indicated that the distribution of
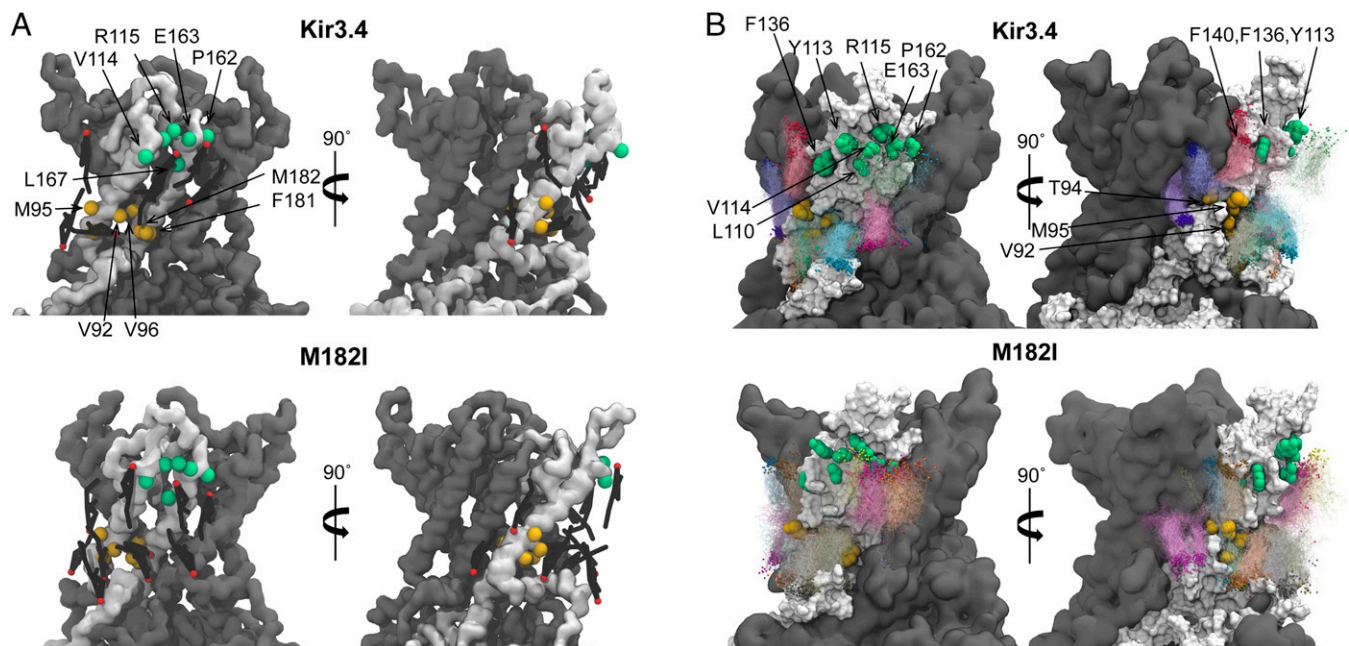
Fig. 2. Interaction of cholesterol with Kir3.4 and the M182I mutant. (*A*) Snapshots showing the cholesterol molecules interacting with each construct in the last frame of the 40-μs-long coarse-grained simulation. For each system, cholesterol molecules with at least one bead within a 0.7-nm cutoff from the backbone of the monomer (shown in white) are represented by black sticks. The polar ROH bead representing the cholesterol hydroxyl group is highlighted by a red sphere. Residues in the outer leaflet contributing to cholesterol binding are shown as green spheres, whereas residues contributing to the interactions with cholesterol in the inner leaflet are shown as yellow spheres. (*B*) Atomistic snapshots showing the cholesterol molecules interacting with each construct during the last 500 ns of the simulation. For each system, all the cholesterol molecules located within a 0.5-nm cutoff from the backbone of the selected monomer (shown as a white surface) are shown as transparent lines every 2.4 ns and colored based on their residue identification. For each cholesterol molecule, the oxygen atom is highlighted as a sphere. Residues in the outer leaflet contributing to cholesterol binding are shown as green spheres, whereas residues contributing to interactions with cholesterol in the inner leaflet are shown as yellow spheres.

POPS lipids in the proximity of the protein coincided with the position of positively charged residues in both the inner and outer membrane leaflets (*SI Appendix*, Fig. S4A). In the outer leaflet, at the interface between adjacent subunits, POPS lipids showed stronger occupancy near K160 of one subunit and polar residues such as S134 and S138 of the neighboring one. In the inner leaflet, K85, R87, and K195 provided an additional interaction site. For the POPE, POPS binary mixture, there was a similar distribution of higher occupancy of POPS lipids around the channel (*SI Appendix*, Fig. S5). This region is highly conserved across Kir channels (e.g., *SI Appendix*, Fig. S1) and has been identified as a phosphatidylinositol 4,5-bisphosphate [PI(4,5)P₂] binding site in functional, crystallographic, and computational studies of a variety of Kir channels (19–24). This site, too, is located at the interface between two adjacent subunits.

With regard to cholesterol, we did not observe substantial differences between Kir3.4 and Kir3.4_M182I in the interaction sites in the outer leaflet (*SI Appendix*, Fig. S4B). In both cases, residues at the extracellular end of the TM helices coordinated with the hydroxyl group of the cholesterol molecule. In one site, electrostatic interactions between the hydroxyl group of cholesterol and charged/polar channel residues (R115 and E163) oriented the hydrophobic moiety of cholesterol downward along the inner and outer TM helices of the same subunit, giving rise to the larger region of high occupancy shown in *SI Appendix*, Fig. S4B. A second interaction site at the extracellular end of the TM helices was located at the interface between the subunits and involved inner TM helix residues of one subunit (e.g., P162) and residues from the neighboring subunit outer TM helix (e.g., F136, V137, and F140), which together trapped the cholesterol molecules along the outer TM helix (*SI Appendix*, Fig. S4B). Cholesterol molecules oriented with the hydroxyl group pointing toward the cytosolic domain further

contributed to the strong cholesterol interaction site along the outer helix (Fig. 2A and *SI Appendix*, Fig. S4B) in both Kir3.4 and its M182I mutant. In contrast, a major difference between the two constructs was observed in the cholesterol interaction sites in the inner leaflet. Specifically, in Kir3.4_M182I, cholesterol hot spots were found in proximity to V96 and F181, close to the interface with the neighboring subunit (Fig. 2A and *SI Appendix*, Fig. S4B). The presence of cholesterol molecules bound to this pocket persisted in the M182I mutant during the 1 μs-long all-atom molecular dynamics (MD) simulation started from the back-mapped structure obtained at the end of the 40 μs-long CG simulation (Fig. 2B). In contrast, only weaker, transient interactions were observed for Kir3.4 in the inner leaflet.

Subsequent to the important observation of the effect of the M182I mutation on the cholesterol distribution in proximity to the channel (Fig. 3A and *SI Appendix*, Fig. S4B), we investigated the local effect of this mutation on channel residues and its propagation throughout the channel. Upon mutation of the methionine to an isoleucine, the side chain at position 182 adopted two distinct rotameric states, thus spanning a wider conformational space (see the histogram of the N-CA-CB-CG dihedral angle of M182 versus those of N-CA-CB-CG1 and N-CA-CB-CG2 of I182) (*SI Appendix*, Fig. S6A).

In the mixture with cholesterol, the differences in local packing induced by the M182I mutation impacted the position of Y97, which shifted closer to the inner TM helix in Kir3.4_M182I, as indicated by the decrease in the distance between the hydroxyl oxygen of Y97 and the backbone carbonyl oxygen of G175 of the same subunit (*SI Appendix*, Fig. S6C). Notably, the subtle change in the orientation of the side chain of Y97 (*SI Appendix*, Fig. S6B) strongly affected the orientation of the side chain of W101 via stacking interactions of
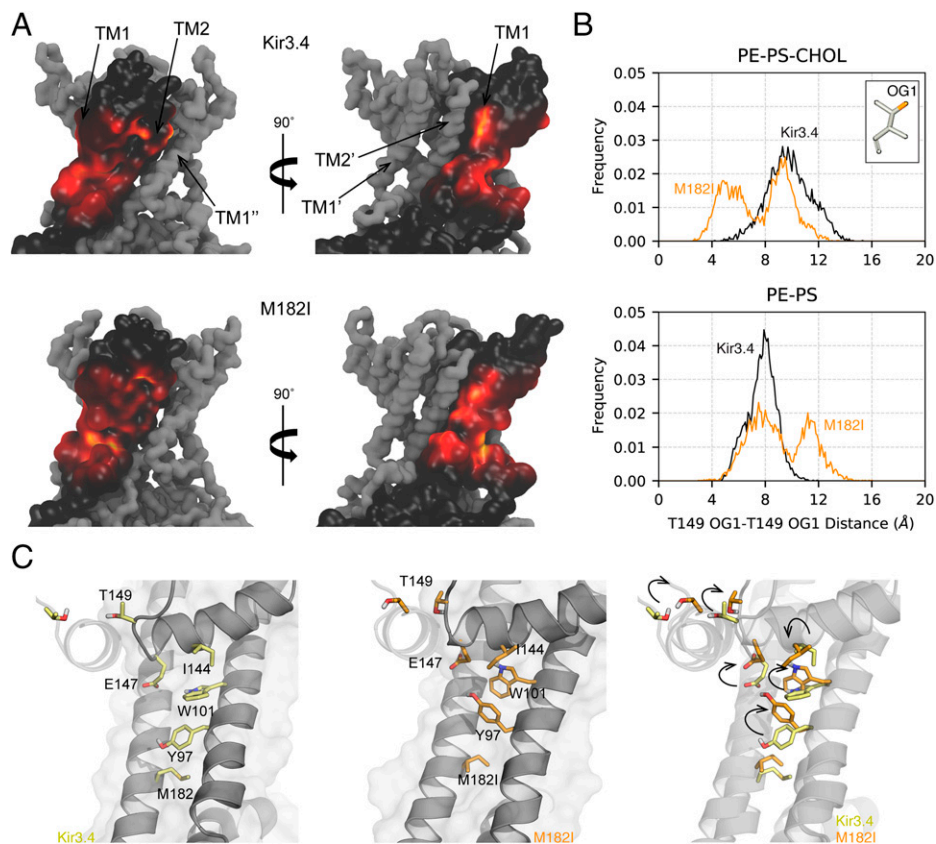
Fig. 3. The impact of the M182I mutation on the Kir3.4 channel and its interaction with cholesterol. (*A*) Occupancy data of cholesterol showing that the M182I mutation affects the distribution of cholesterol in the inner leaflet. For each construct, occupancy data were mapped on the subunit surface using a color scale ranging from black for no or low occupancy to yellow for high occupancy values. To compare Kir3.4 (*Top*) with its M182I mutant (*Bottom*), the highest occupancy value was set to be the same. For clarity, the backbones of the remaining subunits of the tetramer are shown as a gray surface. The outer and inner transmembrane helices (TM1 and TM2, respectively) of the channel subunit and those of the neighboring monomers (TM1', TM1'', and TM2') are highlighted. (*B*) Histograms of the distance between the OG1 atoms of T149 of opposite-facing subunits of Kir3.4 and the M182I mutant embedded in a lipid mixture with (*Upper*) and without (*Lower*) cholesterol. (*C*) Subunit D of the last structure of the all-atom MD simulation in the presence of cholesterol of Kir3.4 (*Left*), Kir3.4_M182I (*Center*), and their overlay (*Right*), showing the propagation of the effect of the M182I mutation from position 182, at the cytosolic side of the inner transmembrane helix, to residue T149 at the selectivity filter.

their aromatic rings. This manifested in the emergence of a dihedral conformation of N-CA-CB-CG1 of W101 in Kir3.4_M182I that did not exist in Kir3.4 (peak centered at −91°) (*SI Appendix*, Fig. S6*D*). This, in turn, extended to affect residues in the pore helix (e.g., I144 and E147), whose side chains were oriented toward the cytosolic domain. In both cases, peaks that existed in Kir3.4 disappeared in Kir3.4_M182I (e.g., the peak in N-CA-CB-CG1 centered at 60° in I144 and the peak in CA-CB-CG-CD centered at −175° in E147) (*SI Appendix*, Fig. S6 *E and F*). The effect on the pore helix propagated to the selectivity filter altering the conformation space of N-CA-CB-CG2 of T149, shifting the center of the peaks at −175° and −73° in Kir3.4 to −160° and −60° in Kir3.4_M182I, respectively (*SI Appendix*, Fig. S6*G*). This change manifested in a critical alteration of the normally distributed distance between the hydroxyl oxygen atoms of T149 residues in diagonally facing subunits. Specifically, whereas Kir3.4 exhibited one peak in the distance distributions centered at 9 Å, a new peak centered at 5 Å appeared in Kir3.4_M182I (Fig. 3*B*).

In the absence of cholesterol, the shift in the Y97-G175 distance was more pronounced (*SI Appendix, Fig. S6C*), whereas only minimal differences in the orientation of W101 between Kir3.4 and Kir3.4_M182I (*SI Appendix*, Fig. S6*D*) were detected. Also, the rotameric states retrieved in Kir3.4 and Kir3.4_M182I for the pore helix residues (I144, E147, and T149) exhibited differential distributions (*SI Appendix*, Fig. S6

E–G). Furthermore, in contrast to the mixture with cholesterol, the distance between T149 residues in diagonally facing subunits increased for Kir3.4_M182I, exhibiting a new peak centered at ∼11 Å (Fig. 3*B*).

Aside from the selectivity filter, two gates have been proposed for Kir channels, the helix bundle crossing at the narrowest part of the TM2 inner helix (F187 in Kir3.4) and the G loop in the cytosolic domain (at M314 and its vicinity in Kir3.4) (25). However, within the time scale of the simulations, no significant changes could be detected at these gates (*SI Appendix*, Fig. S7).

Collectively, these results suggest that conformational changes that occur in proximity to position 182 following the M182I mutation propagate to the selectivity filter of the channel. Crucially, the effect of this mutation on the opening at the selectivity filter is cholesterol dependent. In the presence of cholesterol, the opening at position 149 is decreased, whereas in the absence of cholesterol, it is increased (Fig. 3*B*).

To validate this computational prediction, we investigated the underlying biophysical mechanism. Our prior studies using planar lipid bilayers demonstrated that cholesterol up-regulates Kir3.4* channels by increasing their open probability (26) (Fig. 4*A* and *SI Appendix, Fig. S8A*); no alteration in the conductance (Fig. 4*B*) or surface expression was observed (26). In contrast, an earlier study of Chinese hamster ovary (CHO) cells transfected with Kir2.1 channels detected only a small effect on the open
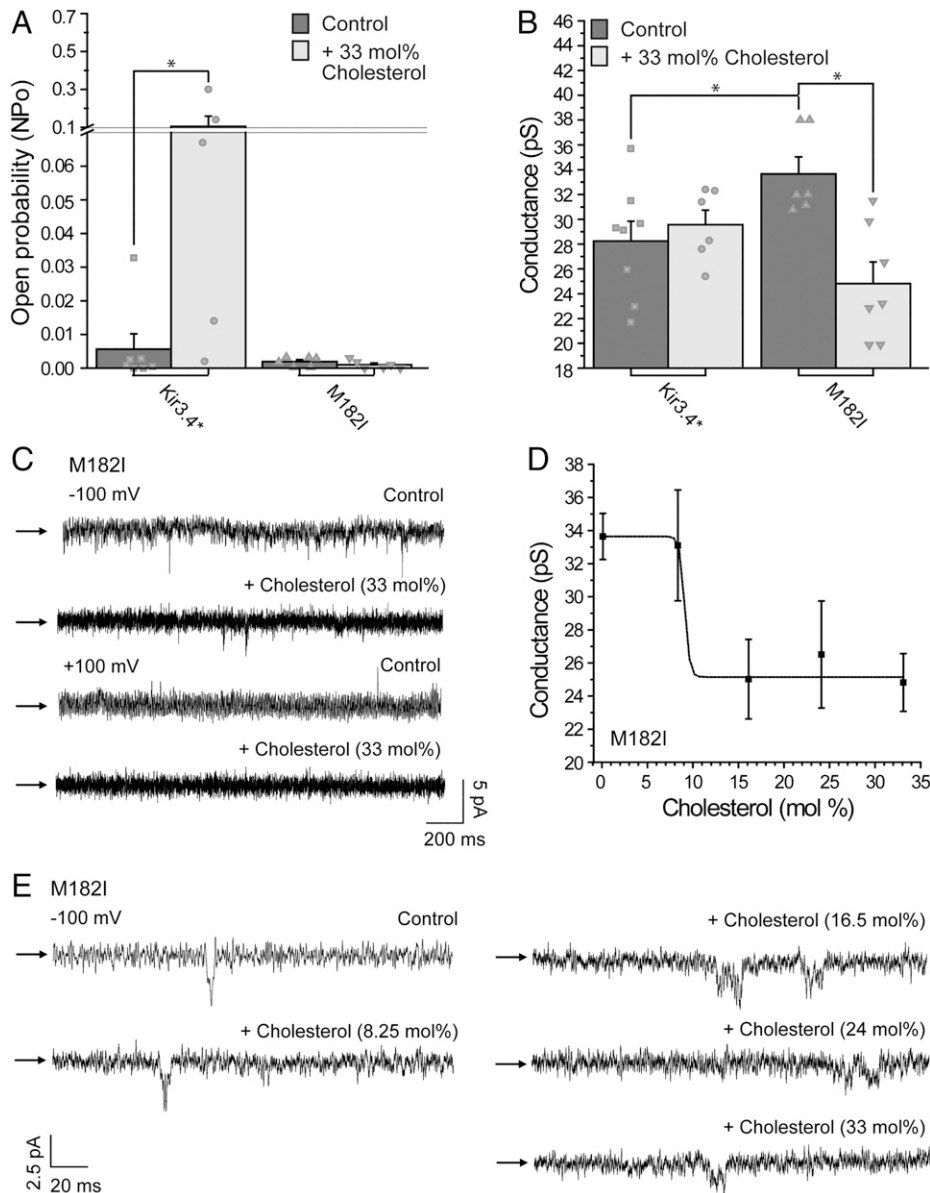
Fig. 4. The M182I mutation leads to a decrease in the conductance of Kir3.4*. (A–E) Reconstitution of Kir3.4* and Kir3.4*_M182I in planar lipid bilayers with varying concentrations of cholesterol, 12.5 μM diC8-PI(4,5)P$_2$, and blocked by 100 nM tertiapin-Q. Significant difference is indicated by an asterisk (*$P \leq$ 0.05). Error bars, SEM. (A) Summary data showing that while 33 mol% cholesterol increases the open probability of Kir3.4* at −100 mV, it does not have a significant effect on the open probability of the M182I mutant (n = 5 to 7). (B) Summary data showing that while 33 mol% cholesterol does not have a significant effect on the conductance of Kir3.4*, it decreases the conductance of Kir3.4*_M182I (n = 6 to 8). (C) Representative traces of Kir3.4*_M182I at −100 and +100 mV. (D) Cholesterol concentration–response curve of the conductance of Kir3.4*_M182I obtained from recordings at single channel resolution (n = 5 to 9). (E) Representative traces of Kir3.4*_M182I reconstituted in lipid bilayers at −100 mV with varying concentrations of cholesterol ranging from 0 mol% (control) to 33 mol%.

probability of the channel by cholesterol (8). As there was also no alteration in the channel's surface expression or unitary conductance, it was proposed that Kir2.1 channels transition from active states to inactive silent states that could not be detected via single channel recordings (8). Thus, to determine the biophysical mechanism by which cholesterol down-regulates the Kir3.4*_M182I mutant, we carried out the following experiments. First, to determine whether cholesterol down-regulates the mutant by decreasing its surface expression, we used total internal reflection fluorescence microscopy (TIRFM) to study the density of eGFP-tagged Kir3.4* and Kir3.4*_M182I channels at the surface of HEK293T cells. As shown in *SI Appendix*, Fig. S9, the surface expression level of both constructs was similar, with or without treatment with cholesterol. Next, we reconstituted the channel

into planar lipid bilayers to determine whether cholesterol down-regulates the Kir3.4*_M182I mutant by altering the open probability or conductance of the channel. This system allows control of the levels of cholesterol, thereby enabling the investigation of the effect of specific cholesterol concentrations on single channel currents (26). We first performed the experiments in the absence and presence of 33 mol% cholesterol. This molar fraction is found in native membranes of mammalian cells (1) and has therefore been previously used for studying cholesterol effects on potassium channels (18, 26, 27). As depicted in Fig. 4 *A–C*, cholesterol did not have a significant effect on the open probability of the Kir3.4*_M182I mutant, but rather caused a significant decrease in the conductance of the channel in agreement with the decreased distance in the selectivity filter (T149) of the M182I

mutant observed in the simulations (Fig. 3B). Compared to the conductance of Kir3.4*, the conductance of Kir3.4*_M182I was higher in the absence of cholesterol and lower in the presence of 33 mol% cholesterol. To further investigate this observation, we determined the cholesterol concentration curve of the conductance of Kir3.4*_M182I by increasing the concentration of cholesterol from 0 mol% to 33 mol%. Notably, a significant reduction in the conductance was observed already at 16.5 mol% cholesterol (Fig. 4 D and E). The identity of the channel at this concentration was confirmed using the Kir3 channel–specific blocker, tertiapin-Q (28) (*SI Appendix*, Fig. S8B).

Discussion

In recent years, a growing number of ion channels has been shown to be down-regulated by cholesterol (4, 5, 8, 29–33). In contrast, only very few have been shown to be up-regulated by this important lipid (6, 7, 34–37). In the current study, we investigated how cholesterol up-regulates Kir3.4* activity. Our work led to the identification of a switch within the TM domain of Kir3.4* that converted the channel from cholesterol up-regulated to down-regulated by reducing the conductance of the channel. Cholesterol down-regulated Kir channels that have a methionine at the equivalent position (e.g., Kir1.1, Kir2.2, and Kir2.3) (5, 8) indicate that this residue is not sufficient to support up-regulation by cholesterol in these channels, suggesting that very specific combinations of residues have evolved to form channels that are up-regulated by cholesterol. Therefore, whereas the mutation of just one residue can convert an up-regulated channel to a down-regulated one, converting a down-regulated channel to an up-regulated one is a complex question, which needs to be investigated separately.

For Kir3.4 and its M182I mutant, extensive coarse-grained simulations followed by all-atom MD simulations and validated experimentally using lipid bilayers pointed to a mechanism comprising two key factors: Alterations in the distribution of cholesterol in the inner leaflet of the membrane in proximity to the channel and propagation of the effect of a single TM point mutation (M182I) located close to the cytosolic domain to decrease the opening at the selectivity filter (T149) of the channel. This is reinforced by the observation of structural changes in the Kir3.4_M182I channel in the absence of cholesterol that described a larger opening at the selectivity filter, possibly linked to the increased conductance detected for the M182I mutant in the planar lipid bilayer experiments lacking cholesterol.

The clear effect of the M182I mutation on the distribution of cholesterol in the inner leaflet (Fig. 3A) suggests that it may be at the core of the effect of this point mutation on the impact of cholesterol on the channel. This notion that alterations in cholesterol distribution may play a key role in determining whether cholesterol would up-regulate or down-regulate Kir channels is further supported by our recent mutagenesis-based electrophysiology studies that suggested a shift in the putative cholesterol binding sites in Kir3.4* compared to Kir2.1 (38). The combined data from the experimental and modeling studies suggest that changes in the propensity for specific cholesterol accumulation in distal TM helices are allosterically coupled to conformational dynamics at the level of the selectivity filter. Interestingly, allosteric coupling between channel function and lipid binding was proposed to be an essential mechanism in the activation of Kir channels by PI(4,5)P$_2$ (19).

The change in the intersubunit distance at the selectivity filter (T149) (Fig. 3B) is supported by our experimental

observation that the conductance of the channel is altered upon the M182I mutation. This conclusion is further supported by studies of the bacterial KcsA potassium channel that was established as a faithful structural model for ion permeation in eukaryotic potassium channels (39). These studies have shown that in its conducting conformation, the permeation pathway of KcsA is ~6 Å wide at its narrowest point (40). Accordingly, the decrease in the intersubunit distance between the hydroxyl oxygen atoms of diagonally facing T149 residues in the presence of cholesterol from ~9 Å in Kir3.4 to ~5 Å in the M182I mutant is expected to have a substantial effect on the conductance of the channel and may underlie the decreased conductance observed in the planar lipid bilayer experiments (Fig. 4). Similarly, in the absence of cholesterol, the increase in the intersubunit distance at the selectivity filter (T149) to ~11 Å in the M182I mutant may underlie the increased conductance observed in bilayers lacking cholesterol.

In summary, our study demonstrates that a single point mutation can invert the impact of cholesterol on an ion channel. Collectively, our data highlight the role of subtle molecular differences in determining how cholesterol distributes in proximity to integral membrane proteins and affects their function. This discovery that, while cholesterol affects the function of Kir3.4 channels, the channels affect the distribution of cholesterol, may open interesting possibilities for specific roles of transmembrane proteins such as Kir channels in organizing membrane lipids.

Materials and Methods

The care of animals (*Xenopus laevis* frogs) and experimental protocols were reviewed and approved by the Animal Care and Use Committees of Virginia Commonwealth University, the University of Tennessee Health Science Center, and Northeastern University. All institutions are accredited by the Association for Assessment and Accreditation of Laboratory Animal Care International.

Expression of Recombinant Channels in *Xenopus* Oocytes. cRNAs were transcribed in vitro using the "Message Machine" kit (Ambion). Oocytes were isolated as described previously (41, 42). Briefly, adult female *Xenopus* laevis frogs were anesthetized in a small container containing 0.1% tricaine methanesulfonate (MS-222) for about 15 min. Subsequently, oocytes were surgically removed through a small abdominal incision. Oocytes were subjected to digestion by collagenase type 7 (~1,000 U/mL; Worthington) until the follicular membrane was removed in ~20% of the oocytes. Expression of channel proteins in *Xenopus* oocytes was accomplished by injection of the desired amount of cRNA, 2 ng of cRNA per oocyte. All oocytes were maintained at 17 °C. Two-electrode voltage clamp recordings were performed 2 d following injection. For harvesting the protein-containing membrane vesicles for lipid bilayer experiments, oocytes were processed as previously described (43, 44).

Cholesterol Enrichment of *Xenopus* Oocytes. Treatment of *Xenopus* oocytes with a mixture of cholesterol and lipids has been shown to increase the cholesterol/phospholipid molar ratio of the plasma membrane of oocytes (45, 46). Thus, in order to enrich the oocytes with cholesterol we used a 1:1:1 (wt/wt/w) mixture containing cholesterol, porcine brain l-α-phosphatidylethanolamine and 1-palmitoyl-2-oleoyl-sn-glycero-3-phospho-l-serine (Avanti Polar Lipids). The mixture was evaporated to dryness under a stream of nitrogen. The resultant pellet was suspended in a buffered solution consisting of 150 mM KCl and 10 mM Tris/Hepes at pH 7.4 and sonicated at 80 kHz in a bath sonicator (Laboratory Supplies). *Xenopus* oocytes were treated with cholesterol for 1 h prior to electrophysiological recordings. This approach results in an ~50% increase in cholesterol levels in oocytes (45, 46), and has been utilized in multiple earlier studies on the cholesterol modulation of Kir channels (5–7, 17, 18, 26, 41, 47, 48). In these studies, the results obtained using the above treatment to enrich oocytes with cholesterol were consistently, in agreement with results obtained using a variety of cell types (e.g., HEK cells, atrial myocytes, and aortic endothelial cells) that

were enriched by using methyl-β-cyclodextrin saturated with cholesterol (6–8, 26, 46, 47, 49–51).

Two-Electrode Voltage Clamp Recording and Analysis. Whole-cell currents were measured by conventional two-microelectrode voltage clamp with a Gene-Clamp 500 amplifier (Molecular Devices [formerly Axon Instruments]), as reported previously (41, 42). A high potassium solution was used to superfuse oocytes: 96 mM KCl, 1 mM NaCl, 1 mM MgCl$_2$, 5 mM KOH/Hepes (pH 7.4). Basal currents represent the difference between inward currents obtained (at −80 mV) in the presence of 3 mM BaCl$_2$ in high-potassium solution and those obtained in the absence of Ba^{2+}. Data are presented as mean ± SEM. Statistical analysis was performed using Origin 7.0 (Originlab). Significance was obtained using a *t* test or one-way ANOVA in accordance with the experimental design. Final plotting of the data was conducted using Origin 7.0 (OriginLab).

Cholesterol Enrichment of HEK293T Cells. HEK293T cells transfected with Kir3.4* or Kir3.4*_M182I were enriched with cholesterol by treatment with methyl-β-cyclodextrin (MβCD) saturated with cholesterol, a well-known cholesterol donor as described previously (46, 52). Briefly, 5 mM MβCD solution in Dulbecco's phosphate-buffered saline (DPBS) mixed with saturated cholesterol at an 8:1 MβCD:cholesterol molar ratio was shaken overnight in a 37 °C incubator. HEK293T cells were incubated with the MβCD solution with cholesterol for 1 h to enhance the cellular cholesterol level.

Surface Expression. Kir3.4* and Kir3.4*_M182I subunits were tagged at the C terminus with eGFP and imaged at the surface of live HEK293T cells by TIRFM. Cells were seeded to #1.5 glass coverslips, transfected, and studied after 24 to 32 h in a bath solution (DPBS with 0.9 mM CaCl$_2$ and 0.49 mM MgCl$_2$). eGFP was excited by a 488-nm laser (Coherent). The beam was conditioned for coherence with custom-built Keplerian beam expanders upstream of a laser cleanup filter (488/10 nm). The laser line was tuned to provide 10 mW of incident light on a micromirror positioned below a high numerical aperture (NA) apochromat objective (60×, 1.5 NA; Olympus) mounted on an RM21 microscope frame equipped with a piezo-driven nano-positioning stage (Mad City Labs). The emission of eGFP was isolated from the excitation beam by an exit micromirror and a ring diagram positioned below the micromirror assembly. The emission beam was passed through a 525/50-nm bandpass filter, then imaged using a back-illuminated sCMOS camera (Teledyne Photometrics) controlled by Micro-Manager freeware (University of California, San Francisco). All filters and mirrors were from Chroma. Lenses, pinholes, and diaphragms were from ThorLabs. Tetra-psec beads (Thermo) were routinely imaged to map the sCMOS chip and to calibrate the evanescent field depth to 100 nm. Particle density was assessed as described previously (53). Briefly, to assess particle density, 16-bit images were captured with a 200-ms exposure time. Following thresholding, fluorescent particles were defined as discrete 3 × 3 pixel regions around a pixel of maximum intensity. Particle number was then counted in ImageJ for a 25-μm^2 region, typically two per cell.

Bilayer Experiments and Analysis. Bilayer experiments were performed as described (18, 26, 43, 54–56). The bilayer lipids, cholesterol, and diC8-PI(4,5)P$_2$ were purchased from Avanti Polar Lipids. All other chemicals were purchased from Sigma-Aldrich. The experimental apparatus consisted of two 1.4-mL chambers separated by a Teflon film that contains a single hole (200 μm in diameter). The bilayer recording solution in both chambers consisted of (in millimoles): 150 KCl, 1 CaCl$_2$, 1 MgCl$_2$, 10-Tris-Hepes, pH 7.4. Bilayer lipids were dissolved in chloroform, then dried under a N$_2$ atmosphere and resuspended in n-decane. A lipid bilayer was formed by "painting" the hole with a 1:1 mixture of L-α-phosphatidylethanolamine and 1-palmitoyl-2-oleoyl-*sn*-glycero-3-[phosphor-L-serine] sodium salt dissolved in n-decane to a final concentration of 5 mg/mL. For experiments with cholesterol, cholesterol powder was first dissolved in chloroform and then added to the lipid mixture to reach the desired concentration. The *cis* side was defined as the chamber connected to the voltage-holding electrode, and all voltages were referenced to the *trans* side (ground) of the chamber. The pellet obtained from the membrane preparation of oocytes expressing the Kir3.4* channel protein was resuspended in 100 μL of bilayer recording solution. After bilayer formation (80 to 120 pF), a 5-μL aliquot of resuspended membrane preparation was added to the *cis* side of the chamber and stirred for several minutes to achieve protein incorporation into the bilayer. The orientation

of the channel insertion was defined by the rectification in response to a set of increasing voltages from −100 mV to +100 mV. Records were low-pass filtered at 1 kHz and sampled at 5 kHz. When needed, the identity of the channel was confirmed by the addition of the selective blocker tertiapin-Q (100 nM) to the chamber corresponding to the extracellular side of the bilayer. Ion currents were obtained for 10 to 60 s of continuous recording using a Warner BC-525D amplifier, Digidata 1322A, and pCLAMP 9.2 software (Molecular Devices). Channel open probability (as a fraction of the time spent in the conducting state) was calculated using the built-in function in Clampfit10.6 software (Molecular Devices) based on the single-channel search option. Before an automatic search for opening events was initiated, the baseline (all channels closed) and opening level 1 were set manually based on the amplitude distribution histogram for each recording. If more than a single level of openings was observed, subsequent levels were set automatically at amplitudes that equaled level 1. During the search, the levels and baseline were updated automatically, while the deltas between them were kept constant. Level contributions were set at 10%. During a single stepping, an event was accepted as an opening if this event's amplitude was equal to or exceeded one-half of the level 1 amplitude. For evaluation of channel conductance, unitary current amplitudes at three to four different voltages were fitted to a linear function. The slope of the resulting fit was used as a measure of conductance. Final data plotting was performed in Origin 8.5.1 (OriginLab). Data are presented as mean ± SEM. Significance was obtained using a *t* test or one-way ANOVA in accordance with the experimental design. Final plotting of the data was conducted using Origin 7.0 (OriginLab).

Preparation of Structures for Molecular Dynamics Simulations. Homology models of Kir3.4 and its M182I mutant were constructed based on the structure of the highly homologous channel Kir3.2 (~70% identity and ~16% similarity), Protein Data Bank (PDB) 3SYA (21). The CHARMM-GUI membrane builder protocol (steps 5 to 7) (57) was used to prepare the protein: 1-palmitoyl-2-oleoyl-glycero-3-phosphocholine (POPC) lipid bilayer complexes solvated in 150 mM KCl aqueous solution using the CHARMM-36 force field for proteins and lipids (58, 59), default NBFIX values for ions (60), and the TIP3P water model (61). The fully assembled systems were equilibrated for 100 ns using NAMD2.10 (62). The resulting fully equilibrated protein structures were used to seed CG MARTINI simulations, as described below.

CG Simulations. The refined homology models of Kir3.4 and the M182I mutant were used as input structures for the CG simulations. The CG simulations were carried out with the Martini force field, version 2.2 for protein and version 2 for lipids (63–65), using GROMACS version 2016.3 (66). For each system, a pipeline based on the martinize.py tool (65), available from the Martini force field website (http://www.cgmartini.nl/), and on the INSANE tool (67) was used to generate a CG representation of the protein and insert it into the membrane, respectively. The pipeline is available for download at: https://github.com/nandhu99/MD_Pipeline. The CG representation of the protein includes an elastic network applied to backbone beads located between 0.5- and 0.9-nm distance, with a force constant of 500 kJ mol^{-1} nm^{-2} (68). The protein was inserted into a 1:1:1 POPE:POPS:cholesterol membrane, resulting in a total of 981 lipids (including 327 cholesterol molecules) for the M182I system, and 978 lipids (including 326 cholesterol molecules) for the Kir3.4 system. For the binary mixture with no cholesterol, we used a 1:1 ratio for POPE:POPS, resulting in 979 lipids per type for both systems. Water molecules and a salt concentration of 0.15 M were added to complete the simulation systems as part of the INSANE procedure (67). Each system was energy minimized first for 10,000 steps using position restraints with a force constant of 1,000 kJ mol^{-1} nm^{-2} on all the protein beads, then for an additional 10,000 steps with position restraints applied only to the backbone beads. The equilibration steps included a 1-ns-long simulation with position restraints on all the protein beads using a time step of 10 fs, followed by 3 additional nanoseconds with a time step of 20 fs. Position restraints were then set in place only for the backbone beads for 3 ns with a force constant of 1,000 kJ mol^{-1} nm^{-2}, and for an additional 3 ns with a force constant of 1 kJ mol^{-1} nm^{-2}. These steps were carried out at 310 K and at 1 bar pressure, using the V-rescale thermostat (with a time constant for coupling of 1 ps) and the Berendsen barostat (69) (with a time constant for pressure coupling of 5 ps). Production runs were performed for a total of 40 μs, with weak position restraints (force constant of 1 kJ mol^{-1} nm^{-2}) applied to the backbone beads,

using a time step of 20 fs, a temperature of 310 K with the V-rescale thermostat and 1 bar pressure, with the Parrinello-Rahman barostat, and a time constant for pressure coupling of 12 ps. All the remaining simulation parameters were those recommended with the latest GROMACS version and included the reaction field potential for the Coulomb interactions (70).

The last frame of each simulation system was mapped back to an atomistic level of detail using the tool BACKWARD (71). For backmapping, only the protein and the lipids of the first few lipid shells were used. For the control systems simulated in the POPE–POPS mixture, this resulted in a total of 325 POPE and 344 POPS lipids for Kir3.4, and 314 POPE and 349 POPS lipids for Kir3.4_M182I. For the systems simulated in the mixture with cholesterol, this resulted in 122 POPE, 145 POPS, and 128 cholesterol molecules for Kir3.4 and 129 POPE, 152 POPS, and 132 cholesterol molecules for the Kir3.4_M182I system.

ANTON2 All-Atom MD Simulations for the Mixture with Cholesterol. The backmapped protein-membrane systems were resolved in 150 mM of KCl and reequilibrated for 100 ns using standard setups of the CHARMM-GUI membrane builder protocol (steps 5 to 7) (72) in the presence of a harmonic restraints acting on heavy protein atoms with the NAMD2.13 software package (73). The CHARMM36M and updated CHARMM36 force fields were used for protein and lipids, respectively (59, 74). The water was modeled with a TIP3P potential (61) and ion parameters included NBFIX corrections (60). Production runs were performed for 1 μs for both the Kir3.4 and M182I systems. The production runs were executed in a semi-isotropic (NPaT) ensemble at temperature 315 K maintained by the Nosé–Hoover thermostat (75). The time step for the production runs was set to 2 fs and the trajectories were saved every 240 ps. Nonbonded and long-range electrostatic interactions were evaluated every 2 and 6 fs, respectively. Long-range electrostatics were calculated using the k-Gaussian Ewald method implemented to enhance performance on the ANTON2 platform (76, 77) with a $64 \times 64 \times 64$ grid. SHAKE was used to constrain all bonds involving hydrogen atoms.

All-Atom MD Simulations for the Control Systems without Cholesterol. The back-mapped membrane-protein systems were resolved in 150 mM of KCl and equilibrated for a total of 150 ns, including 60 ns with position restraints on all the protein heavy atoms, followed by 20 ns with position restraints applied to the backbone and β-carbon atoms of the proteins and by an additional 20 ns with position restraints applied only to the backbone atoms. Next, a 50-ns equilibration step was performed with position restraints only on the α-carbon atoms. The force constant of the position restraints was set at 1,000 kJ mol^{-1} nm^{-2}. All the equilibration steps were performed with GROMACS v.2018.7 (66) and the February 2021 release of the CHARMM36 force fields, available from the MacKerell laboratory at http://mackerell.umaryland.edu/charmm_ff.shtml#gromacs, with the TIP3P water model (59, 74, 78). The temperature was maintained at 315 K using the Berendsen thermostat (69), with a relaxation time of 1 ps. Semiisotropic pressure coupling was applied with the Berendsen barostat (69), using a relaxation time of 5 ps, to maintain the pressure at 1 bar. The LINCS algorithm was employed to constrain H-atom bonds (79). We used the Verlet cutoff scheme for neighbor searching, with van der Waals interactions switched to 0 between 1 and 1.2 nm. Long-range electrostatic interactions were treated using the particle mesh Ewald algorithm (80, 81). Production runs were performed for each system for 1 μs with no position restraints, using the Nosé–Hoover thermostat (82, 83), with a relaxation time of 1 ps, and the Parrinello–Rahman barostat (84), with a relaxation time of 12 ps. Temperature was maintained at 315 K and the pressure at 1 bar. Trajectories were saved every 240 ps.

Computational Analyses.

1) Lipid count analysis. The composition of the first lipid shell was approximated to the number of lipids found within a 0.7-nm cutoff from the protein, as was done in previous studies (85, 86). For POPE and POPS lipids we counted the number of PO4 beads, while for cholesterol we used as a reference the polar ROH bead representing the cholesterol hydroxyl group. The analysis was carried out during the last 20 μs of the simulation, using the tool *gmx select* available as part of the GROMACS package. The Matplotlib (87) and NumPy (88) libraries were used for plotting the results.

2) Occupancy maps analysis for POPS and cholesterol. Fractional occupancy maps for POPS and cholesterol were calculated using the VolMap plugin in VMD 1.9.3 with a grid resolution of 1 Å (89). For each simulation system, the last 20 μs were considered. From this, four different subsystem trajectories were created, each containing only one of the four monomers and the lipids. The four monomeric subsystems were then aligned using progressive fitting based on the backbone beads. The fractional occupancy maps were calculated within a 15-Å cutoff from the protein backbone beads, using the fitted trajectory. This approach provides the advantage of averaging the occupancy over four monomers at a time, for each system. The POPS maps are shown at isosurfaces drawn at 30% and 60% of the maximum occupancy value, which for each lipid species is common to all systems. Cholesterol isosurfaces were drawn at 30% and 70% of a maximum occupancy value set to be the same for both systems. The maps are superimposed with the protein structure corresponding to the last frame of each simulation.

3) Distances. Interchain distances between pairs of T149(OG1) atoms belonging to opposite monomers (i.e., chains A, C and chains B, D) and intrachain distances between pairs of Y97(OH)-G175(O) atoms per monomer were calculated using CHARMM scripts (v44b2). The last 700 ns–totaling 2,917 frames–of Kir3.4 and the M182I mutant trajectories were considered for the analysis. Histograms were obtained for each time series using 0.1-Å bin size from 0 to 20 Å and then averaged among all time series [two for T149(OG1)-T149 (OG1) and four for the Y97(OH)-G175(O) atom pairs].

4) Dihedrals. For each monomer, dihedral angles were calculated for the residues Y97, W101, I144, E147, T149, and M/I182 using the CHARMM Correl module (v44b2) (90). The last 700 ns–totaling 2,917 frames–of Kir3.4 and M182I mutant trajectories were considered for the analysis. Histograms were obtained for each time series using 1.0° bin size from −180° to 180° and then averaged among all time series (four per residue).

5) Figures. Figures of the molecular models were generated with VMD 1.9.1 and VMD 1.9.3 (89), the PyMOL Molecular Graphics System (version 2.0, Schrödinger, LLC), and Discovery Studio 3.1 Visualizer (Biovia [formerly Accelrys]).

Data Availability. All study data are included in the article and/or *SI Appendix*.

Author affiliations: ^aCentre for Molecular Simulation, University of Calgary, Calgary, AB T2N 1N4, Canada; ^bDepartment of Biological Sciences, University of Calgary, Calgary, AB T2N 1N4, Canada; ^cDepartment of Pharmacology, Addiction Science, and Toxicology, The University of Tennessee Health Science Center, Memphis, TN 38163; ^dDepartment of Pharmaceutical Sciences, School of Pharmacy, Bouvé College of Health Sciences, Northeastern University, Boston, MA 02115; ^eDepartment of Physiology and Biophysics, Virginia Commonwealth University School of Medicine, Richmond, VA 23298; and ^fDepartment of Chemistry, University of Illinois at Chicago, Chicago, IL 60607

1. G. Gimpl, K. Burger, F. Fahrenholz, Cholesterol as modulator of receptor function. *Biochemistry* **36**, 10959–10974 (1997).

2. P. Goluszko, B. Nowicki, Membrane cholesterol: A crucial molecule affecting interactions of microbial pathogens with mammalian cells. *Infect. Immun.* **73**, 7791–7796 (2005).

3. O. G. Ramprasad et al., Changes in cholesterol levels in the plasma membrane modulate cell signaling and regulate cell adhesion and migration on fibronectin. *Cell Motil. Cytoskeleton* **64**, 199–216 (2007).

4. A. Rosenhouse-Dantsker, D. Mehta, I. Levitan, Regulation of ion channels by membrane lipids. *Compr. Physiol.* **2**, 31–68 (2012).

5. A. Rosenhouse-Dantsker, E. Leal-Pinto, D. E. Logothetis, I. Levitan, Comparative analysis of cholesterol sensitivity of Kir channels: Role of the CD loop. *Channels (Austin)* **4**, 63–66 (2010).

6. W. Deng et al., Hypercholesterolemia induces up-regulation of K$_{ACh}$ cardiac currents via a mechanism independent of phosphatidylinositol 4,5-bisphosphate and G$\beta\gamma$. *J. Biol. Chem.* **287**, 4925–4935 (2012).

7. A. N. Bukiya, S. Durdagi, S. Noskov, A. Rosenhouse-Dantsker, Cholesterol up-regulates neuronal G protein-gated inwardly rectifying potassium (GIRK) channel activity in the hippocampus. *J. Biol. Chem.* **292**, 6135–6147 (2017).

8. V. G. Romanenko *et al.*, Cholesterol sensitivity and lipid raft targeting of Kir2.1 channels. *Biophys. J.* **87**, 3850–3861 (2004).

9. H. Hibino *et al.*, Inwardly rectifying potassium channels: Their structure, function, and physiological roles. *Physiol. Rev.* **90**, 291–366 (2010).

10. N. Dascal *et al.*, Atrial G protein-activated K$^+$ channel: Expression cloning and molecular properties. *Proc. Natl. Acad. Sci. U.S.A.* **90**, 10235–10239 (1993).

11. Y. Kubo, T. J. Baldwin, Y. N. Jan, L. Y. Jan, Primary structure and functional expression of a mouse inward rectifier potassium channel. *Nature* **362**, 127–133 (1993).

12. M. Nishida, M. Cadene, B. T. Chait, R. MacKinnon, Crystal structure of a Kir3.1-prokaryotic Kir channel chimera. *EMBO J.* **26**, 4005–4015 (2007).

13. X. Tao, J. L. Avalos, J. Chen, R. MacKinnon, Crystal structure of the eukaryotic strong inward-rectifier K$^+$ channel Kir2.2 at 3.1 A resolution. *Science* **326**, 1668–1674 (2009).

14. K. P. K. Lee, J. Chen, R. MacKinnon, Molecular structure of human KATP in complex with ATP and ADP. *eLife* **6**, e32481 (2017).

15. K. W. Chan, J. L. Sui, M. Vivaudou, D. E. Logothetis, Control of channel activity through a unique amino acid residue of a G protein-gated inwardly rectifying K$^+$ channel subunit. *Proc. Natl. Acad. Sci. U.S.A.* **93**, 14193–14198 (1996).

16. M. Vivaudou *et al.*, Probing the G-protein regulation of GIRK1 and GIRK4, the two subunits of the K$_{ACh}$ channel, using functional homomeric mutants. *J. Biol. Chem.* **272**, 31553–31560 (1997).

17. A. Rosenhouse-Dantsker, S. Noskov, S. Durdagi, D. E. Logothetis, I. Levitan, Identification of novel cholesterol-binding regions in Kir2 channels. *J. Biol. Chem.* **288**, 31154–31164 (2013).

18. A. N. Bukiya, A. Rosenhouse-Dantsker, Synergistic activation of G protein-gated inwardly rectifying potassium channels by cholesterol and PI(4,5)P$_2$. *Biochim. Biophys. Acta Biomembr.* **1859**, 1233–1241 (2017).

19. C. M. Lopes *et al.*, Alterations in conserved Kir channel-PIP2 interactions underlie channelopathies. *Neuron* **34**, 933–944 (2002).

20. A. Rosenhouse-Dantsker, D. E. Logothetis, Molecular characteristics of phosphoinositide binding. *Pflugers Arch.* **455**, 45–53 (2007).

21. M. R. Whorton, R. MacKinnon, Crystal structure of the mammalian GIRK2 K$^+$ channel and gating regulation by G proteins, PIP2, and sodium. *Cell* **147**, 199–208 (2011).

22. X. Y. Meng, H. X. Zhang, D. E. Logothetis, M. Cui, The molecular mechanism by which PIP(2) opens the intracellular G-loop gate of a Kir3.1 channel. *Biophys. J.* **102**, 2049–2059 (2012).

23. D. E. Logothetis *et al.*, Unifying mechanism of controlling Kir3 channel activity by G proteins and phosphoinositides. *Int. Rev. Neurobiol.* **123**, 1–26 (2015).

24. I. W. Glaaser, P. A. Slesinger, Structural insights into GIRK Channel function. *Int. Rev. Neurobiol.* **123**, 117–160 (2015).

25. D. Li, T. Jin, D. Gazgalis, M. Cui, D. E. Logothetis, On the mechanism of GIRK2 channel gating by phosphatidylinositol bisphosphate, sodium, and the G$\beta\gamma$ dimer. *J. Biol. Chem.* **294**, 18934–18948 (2019).

26. A. N. Bukiya *et al.*, Cholesterol increases the open probability of cardiac K$_{ACh}$ currents. *Biochim. Biophys. Acta* **1848**, 2406–2413 (2015).

27. J. J. Crowley, S. N. Treistman, A. M. Dopico, Cholesterol antagonizes ethanol potentiation of human brain BK$_{Ca}$ channels reconstituted into phospholipid bilayers. *Mol. Pharmacol.* **64**, 365–372 (2003).

28. H. Kitamura *et al.*, Tertiapin potently and selectively blocks muscarinic K($^+$) channels in rabbit cardiac myocytes. *J. Pharmacol. Exp. Ther.* **293**, 196–205 (2000).

29. V. Bolotina, V. Omelyanenko, B. Heyes, U. Ryan, P. Bregestovski, Variations of membrane cholesterol alter the kinetics of Ca2($^+$)-dependent K$^+$ channels and membrane fluidity in vascular smooth muscle cells. *Pflugers Arch.* **415**, 262–268 (1989).

30. A. M. Dopico, A. N. Bukiya, A. K. Singh, Large conductance, calcium- and voltage-gated potassium (BK) channels: Regulation by cholesterol. *Pharmacol. Ther.* **135**, 133–150 (2012).

31. C. C. Wu *et al.*, The effect of hypercholesterolemia on the sodium inward currents in cardiac myocyte. *J. Mol. Cell. Cardiol.* **27**, 1263–1269 (1995).

32. M. Toselli, G. Biella, V. Taglietti, E. Cazzaniga, M. Parenti, Caveolin-1 expression and membrane cholesterol content modulate N-type calcium channel activity in NG108-15 cells. *Biophys. J.* **89**, 2443–2457 (2005).

33. I. Levitan, A. E. Christian, T. N. Tulenko, G. H. Rothblat, Membrane cholesterol content modulates activation of volume-regulated anion current in bovine endothelial cells. *J. Gen. Physiol.* **115**, 405–416 (2000).

34. T. P. Lockwich *et al.*, Assembly of Trp1 in a signaling complex associated with caveolin-scaffolding lipid raft domains. *J. Biol. Chem.* **275**, 11934–11942 (2000).

35. V. I. Chubinskiy-Nadezhdin, Y. A. Negulyaev, E. A. Morachevskaya, Cholesterol depletion-induced inhibition of stretch-activated channels is mediated via actin rearrangement. *Biochem. Biophys. Res. Commun.* **412**, 80–85 (2011).

36. V. G. Shlyonsky, F. Mies, S. Sariban-Sohraby, Epithelial sodium channel activity in detergent-resistant membrane microdomains. *Am. J. Physiol. Renal Physiol.* **284**, F182–F188 (2003).

37. M. S. Awayda *et al.*, Acute cholesterol-induced anti-natriuretic effects: Role of epithelial Na$^+$ channel activity, protein levels, and processing. *J. Biol. Chem.* **286**, 1683–1695 (2011).

38. A. Rosenhouse-Dantsker, Cholesterol binding sites in inwardly rectifying potassium channels. *Adv. Exp. Med. Biol.* **1135**, 119–138 (2019).

39. M. LeMasurier, L. Heginbotham, C. Miller, KcsA: It's a potassium channel. *J. Gen. Physiol.* **118**, 303–314 (2001).

40. D. Meuser, H. Splitt, R. Wagner, H. Schrempf, Exploring the open pore of the potassium channel from *Streptomyces lividans*. *FEBS Lett.* **462**, 447–452 (1999).

41. A. Rosenhouse-Dantsker, D. E. Logothetis, I. Levitan, Cholesterol sensitivity of KIR2.1 is controlled by a belt of residues around the cytosolic pore. *Biophys. J.* **100**, 381–389 (2011).

42. C. He *et al.*, Identification of critical residues controlling G protein-gated inwardly rectifying K($^+$) channel activity through interactions with the $\beta\gamma$ subunits of G proteins. *J. Biol. Chem.* **277**, 6088–6096 (2002).

43. E. Leal-Pinto *et al.*, Gating of a G protein-sensitive mammalian Kir3.1 prokaryotic Kir channel chimera in planar lipid bilayers. *J. Biol. Chem.* **285**, 39790–39800 (2010).

44. A. Aleksandrov, B. Velimirovic, D. E. Clapham, Inward rectification of the IRK1 K$^+$ channel reconstituted in lipid bilayers. *Biophys. J.* **70**, 2680–2687 (1996).

45. J. Santiago *et al.*, Probing the effects of membrane cholesterol in the *Torpedo californica* acetylcholine receptor and the novel lipid-exposed mutation alpha C418W in *Xenopus* oocytes. *J. Biol. Chem.* **276**, 46523–46532 (2001).

46. A. Slayden *et al.*, Enrichment of mammalian tissues and *Xenopus* oocytes with cholesterol. *J. Vis. Exp.* **157**, 10.3791/60734 (2020).

47. A. Rosenhouse-Dantsker *et al.*, Distant cytosolic residues mediate a two-way molecular switch that controls the modulation of Kir channels by cholesterol and PI(4,5)P$_2$. *J. Biol. Chem.* **287**, 40266–40278 (2012).

48. A. Rosenhouse-Dantsker, S. Noskov, D. E. Logothetis, I. Levitan, Cholesterol sensitivity of KIR2.1 depends on functional inter-links between the N and C termini. *Channels (Austin)* **7**, 303–312 (2013).

49. V. G. Romanenko, G. H. Rothblat, I. Levitan, Modulation of endothelial inward-rectifier K$^+$ current by optical isomers of cholesterol. *Biophys. J.* **83**, 3211–3222 (2002).

50. Y. Fang *et al.*, Hypercholesterolemia suppresses inwardly rectifying K$^+$ channels in aortic endothelium in vitro and in vivo. *Circ. Res.* **98**, 1064–1071 (2006).

51. E. R. Mohler III *et al.*, Hypercholesterolemia suppresses Kir channels in porcine bone marrow progenitor cells in vivo. *Biochem. Biophys. Res. Commun.* **358**, 317–324 (2007).

52. A. E. Christian, M. P. Haynes, M. C. Phillips, G. H. Rothblat, Use of cyclodextrins for manipulating cellular cholesterol content. *J. Lipid Res.* **38**, 2264–2272 (1997).

53. L. D. Plant, D. Xiong, J. Romero, H. Dai, S. A. N. Goldstein, Hypoxia produces pro-arrhythmic late sodium current in cardiac myocytes by SUMOylation of Na$_V$1.5 channels. *Cell Rep.* **30**, 2225–2236.e4 (2020).

54. A. N. Bukiya, T. Vaithianathan, L. Toro, A. M. Dopico, The second transmembrane domain of the large conductance, voltage- and calcium-gated potassium channel beta(1) subunit is a lithocholate sensor. *FEBS Lett.* **582**, 673–678 (2008).

55. A. N. Bukiya, J. D. Belani, S. Rychnovsky, A. M. Dopico, Specificity of cholesterol and analogs to modulate BK channels points to direct sterol-channel protein interactions. *J. Gen. Physiol.* **137**, 93–110 (2011).

56. A. K. Singh *et al.*, Multiple cholesterol recognition/interaction amino acid consensus (CRAC) motifs in cytosolic C tail of Slo1 subunit determine cholesterol sensitivity of Ca^{2+}- and voltage-gated K$^+$ (BK) channels. *J. Biol. Chem.* **287**, 20509–20521 (2012).

57. S. Jo, J. B. Lim, J. B. Klauda, W. Im, CHARMM-GUI Membrane Builder for mixed bilayers and its application to yeast membranes. *Biophys. J.* **97**, 50–58 (2009).

58. R. B. Best *et al.*, Optimization of the additive CHARMM all-atom protein force field targeting improved sampling of the backbone φ, ψ and side-chain χ(1) and χ(2) dihedral angles. *J. Chem. Theory Comput.* **8**, 3257–3273 (2012).

59. J. B. Klauda *et al.*, Update of the CHARMM all-atom additive force field for lipids: Validation on six lipid types. *J. Phys. Chem. B* **114**, 7830–7843 (2010).

60. S. Y. Noskov, B. Roux, Control of ion selectivity in LeuT: Two Na$^+$ binding sites with two different mechanisms. *J. Mol. Biol.* **377**, 804–818 (2008).

61. W. L. Jorgensen, J. Chandrasekhar, J. D. Madura, R. W. Impey, M. L. Klein, Comparison of simple potential functions for simulating liquid water. *J. Chem. Phys.* **79**, 926–935 (1983).

62. J. C. Phillips *et al.*, Scalable molecular dynamics on CPU and GPU architectures with NAMD. *J. Chem. Phys.* **153**, 044130 (2020).

63. S. J. Marrink, H. J. Risselada, S. Yefimov, D. P. Tieleman, A. H. de Vries, The MARTINI force field: Coarse grained model for biomolecular simulations. *J. Phys. Chem. B* **111**, 7812–7824 (2007).

64. L. Monticelli *et al.*, The MARTINI coarse-grained force field: Extension to proteins. *J. Chem. Theory Comput.* **4**, 819–834 (2008).

65. D. H. de Jong *et al.*, Improved parameters for the martini coarse-grained protein force field. *J. Chem. Theory Comput.* **9**, 687–697 (2013).

66. M. J. Abraham *et al.*, Gromacs: High performance molecular simulations through multi-level parallelism from laptops to supercomputers. *SoftwareX* **1–2**, 19–25 (2015).

67. T. A. Wassenaar, H. I. Ingólfsson, R. A. Böckmann, D. P. Tieleman, S. J. Marrink, Computational lipidomics with insane: A versatile tool for generating custom membranes for molecular simulations. *J. Chem. Theory Comput.* **11**, 2144–2155 (2015).

68. X. Periole, M. Cavalli, S. J. Marrink, M. A. Ceruso, Combining an elastic network with a coarse-grained molecular force field: Structure, dynamics, and intermolecular recognition. *J. Chem. Theory Comput.* **5**, 2531–2543 (2009).

69. H. J. C. Berendsen, J. P. M. Postma, W. F. van Gunsteren, A. DiNola, J. R. Haak, Molecular dynamics with coupling to an external bath. *J. Chem. Phys.* **81**, 3684–3690 (1984).

70. D. H. de Jong, S. Baoukina, H. I. Ingolfsson, S. J. Marrink, Martini straight: Boosting performance using a shorter cutoff and GPUs. *Comput. Phys. Commun.* **199**, 1–7 (2016).

71. T. A. Wassenaar, K. Pluhackova, R. A. Böckmann, S. J. Marrink, D. P. Tieleman, Going backward: A flexible geometric approach to reverse transformation from coarse grained to atomistic models. *J. Chem. Theory Comput.* **10**, 676–690 (2014).

72. E. L. Wu *et al.*, CHARMM-GUI Membrane Builder toward realistic biological membrane simulations. *J. Comput. Chem.* **35**, 1997–2004 (2014).

73. J. C. Phillips *et al.*, Scalable molecular dynamics with NAMD. *J. Comput. Chem.* **26**, 1781–1802 (2005).

74. J. Huang *et al.*, CHARMM36m: An improved force field for folded and intrinsically disordered proteins. *Nat. Methods* **14**, 71–73 (2017).

75. G. J. Martyna, D. J. Tobias, M. L. Klein, Constant-pressure molecular-dynamics algorithms. *J. Chem. Phys.* **101**, 4177–4189 (1994).

76. Y. Shan, J. L. Klepeis, M. P. Eastwood, R. O. Dror, D. E. Shaw, Gaussian split Ewald: A fast Ewald mesh method for molecular simulation. *J. Chem. Phys.* **122**, 54101 (2005).

77. D. E. Shaw *et al.*, *Anton 2: Raising the Bar for Performance and Programmability in a Special-Purpose Molecular Dynamics Supercomputer* (IEEE Press, 2014), pp. 41–53.

78. P. Bjelkmar, P. Larsson, M. A. Cuendet, B. Hess, E. Lindahl, Implementation of the charmm force field in GROMACS: Analysis of protein stability effects from correction maps, virtual interaction sites, and water models. *J. Chem. Theory Comput.* **6**, 459–466 (2010).

79. B. Hess, H. Bekker, H. J. C. Berendsen, J. G. E. M. Fraaije, LINCS: A linear constraint solver for molecular simulations. *J. Comput. Chem.* **18**, 1463–1472 (1997).

80. T. Darden, D. York, L. Pedersen, Particle mesh Ewald: An N-log(N) method for Ewald sums in large systems. *J. Chem. Phys.* **98**, 10089–10092 (1993).

81. U. Essmann *et al.*, A smooth particle mesh Ewald method. *J. Chem. Phys.* **103**, 8577–8593 (1995).

82. W. G. Hoover, Canonical dynamics: Equilibrium phase-space distributions. *Phys. Rev. A Gen. Phys.* **31**, 1695–1697 (1985).

83. S. Nosé, A molecular dynamics method for simulations in the canonical ensemble. *Mol. Phys.* **25**, 255–268 (1984).

84. M. Parrinello, A. Rahman, Polymorphic transitions in single crystals: A new molecular dynamics method. *J. Appl. Phys.* **52**, 7182–7190 (1981).

85. V. Corradi *et al.*, Lipid-protein interactions are unique fingerprints for membrane proteins. *ACS Cent. Sci.* **4**, 709–717 (2018).

86. S. Mehmood *et al.*, Structural and functional basis for lipid synergy on the activity of the antibacterial peptide ABC transporter McjD. *J. Biol. Chem.* **291**, 21656–21668 (2016).

87. J. D. Hunter, Matplotlib: A 2D graphics environment. *Comput. Sci. Eng.* **9**, 90–95 (2007).

88. C. R. Harris *et al.*, Array programming with NumPy. *Nature* **585**, 357–362 (2020).

89. W. Humphrey, A. Dalke, K. Schulten, VMD: Visual molecular dynamics. *J. Mol. Graph.* **14**, 33–38, 27–28 (1996).

90. B. R. Brooks *et al.*, CHARMM: The biomolecular simulation program. *J. Comput. Chem.* **30**, 1545–1614 (2009).